

Article

Preparation of New Sm-Doped CuO/ZnO/CuMn₂O₄ Tri-Composite for Photoremoval of Dissolved Organic Waste and Dielectric-Energy Storage

Hanan A. Althikrallah ^{1,*}, Ghayah M. Alsulaim ^{1,*}, Shada A. Alsharif ² and Kholoud M. Alnahdi ³¹ Department of Chemistry, College of Science, King Faisal University, Al Ahsa 31982, Saudi Arabia² University College of Umluj, University of Tabuk, Tabuk 71491, Saudi Arabia; shalsharif@ut.edu.sa³ Department of Physics, Faculty of Science, University of Tabuk, Tabuk 71491, Saudi Arabia; kalnahdi@ut.edu.sa

* Correspondence: galsaleem@kfu.edu.sa (G.M.A.); halhekrallh@kfu.edu.sa (H.A.A.)

Abstract: Photocatalysis is considered as simple, green, and the best strategy for elimination of hazardous organic contaminants from wastewater. Herein, new broad spectrum photocatalysts based on pure and Sm-doped CuO/ZnO/CuMn₂O₄ ternary composites were simply prepared by co-precipitation approach. The X-ray diffraction results proved the formation of a composite structure. The transmission electron microscope (TEM) images displayed that most particles have a spherical shape with average mean sizes within 26–29 nm. The optical properties of both samples signified that the addition of Sm ions significantly improves the harvesting of the visible light spectrum of CuO/ZnO/CuMn₂O₄ ternary composites. The photocatalytic study confirmed that 97% of norfloxacin and 96% of methyl green pollutants were photo-degraded in the presence of the Sm-doped CuO/ZnO/CuMn₂O₄ catalyst after 50 and 40 min, respectively. The total organic carbon analysis revealed the high mineralization efficiency of the Sm-doped CuO/ZnO/CuMn₂O₄ catalyst to convert the norfloxacin and methyl green to carbon dioxide and water molecules. During three cycles, this catalyst presented a high removal efficiency for norfloxacin and methyl green contaminants. As a dielectric energy storage material, the Sm-doped CuO/ZnO/CuMn₂O₄ ternary composite has large dielectric constant values, mainly at low frequencies, with low dielectric loss compared to a pure CuO/ZnO/CuMn₂O₄ composite.

Keywords: ternary composite; rare-earth; broad spectrum photocatalyst; antibiotics and dyes; electrical conductivity and dielectric properties



Citation: Althikrallah, H.A.; Alsulaim, G.M.; Alsharif, S.A.; Alnahdi, K.M. Preparation of New Sm-Doped CuO/ZnO/CuMn₂O₄ Tri-Composite for Photoremoval of Dissolved Organic Waste and Dielectric-Energy Storage. *J. Compos. Sci.* **2024**, *8*, 152. <https://doi.org/10.3390/jcs8040152>

Academic Editor: Francesco Tornabene

Received: 23 March 2024

Revised: 9 April 2024

Accepted: 12 April 2024

Published: 18 April 2024



Copyright: © 2024 by the authors. Licensee MDPI, Basel, Switzerland. This article is an open access article distributed under the terms and conditions of the Creative Commons Attribution (CC BY) license (<https://creativecommons.org/licenses/by/4.0/>).

1. Introduction

For a healthy and safe environment, efficient treatment of dissolved organic compounds such as dyes, antibiotics, fungicides, insecticides, and herbicides has gained great attention in current scientific research [1–3]. Polluted water is one of the most important environmental problems; wherein numerous poisonous and continual organic contaminants pose a high threat to living organisms [4,5]. Antibiotics are important drugs for human and animals which are widely reported in water resources as pharmaceutical contaminants [6]. It was reported that the consumption of antibiotics ranges from 100,000 to 200,000 tons annually [6]. Norfloxacin (C₁₆H₁₈FN₃O₃) compound is one of the first third generation fluoroquinolone antibiotics that has been broadly used to damage the broad-spectrum of Gram negative and some Gram positive bacteria [7–9]. But, a major part of the norfloxacin antibiotic nurtured to save poultry is excreted without breakdown, spread in soil enhanced by animal manure, and finally enters water resources, causing harmful effects to human and aquatic organisms in water. Additionally, norfloxacin can also cause damage to human kidneys, as well as delay the formation of bones in minors, affecting normal development, and most countries have cautioned minors from taking it [7–11].

Organic dyes such as Congo red, methylene blue, and methyl green are another family of industrial compounds which are frequently be present in wastewater [12,13]. Every year, nearly 7×10^7 tons of industrial dyes are used, and many of these compounds contain harmful chemicals that are hazardous for the environment and human health [14,15]. Most of the synthesized organic dyes are very stable under heat and light effects; therefore, they are not ecofriendly and non-biodegradable [16,17]. Methyl green (MG) is a triphenylmethane-type cationic dye, broadly used in the textile industry, medicine, and biology [18,19]. It is highly hazardous and the existence of methyl green in the water resources is a great worry owing to its potential poisonousness to the aquatic system and all organisms [18,19]. In view of that, it is very important to use an efficient method to effectively remove organic pollutants such as norfloxacin and methyl green from wastewater. Considering this, photocatalysis is a green, simple, low cost and effective methodology that illuminates great benefits for the elimination of organic contaminants from wastewater [20,21]. Based on coupling between different oxides in ternary composites, a new strategy has emerged to improve the photoresponse and increase the harvesting of visible light spectrum, as well as support the separation of the charge carriers which trigger photocatalytic efficiency [22–24]. Ali et al. [25] studied the photocatalytic properties of BiOBr/ZnO/WO₃ ternary nanocomposites for degradation of phenol. The authors found that this composite has a degradation efficiency of 90% for 50 mg/L phenol under visible-light illumination for 300 min. A ternary ZnO/Fe₃O₄/g-C₃N₄ composite synthesized using the hydrothermal method exhibited removal efficiencies of 97.87, 98.05, and 83.35% for methyl orange, alizarin yellow R, and orange G dyes in 150 min of visible light irradiation [26]. Liu et al. [27] reported that the In₂O₃/ZnO@Ag nanowire ternary composite has a visible light photodegradation efficiency of 92% for 4-nitrophenol in 240 min and 93% for methyl orange in 90 min.

The n-type ZnO and the p-type CuO semiconductors are well-known and strong candidates for photocatalysts for wastewater treatment [28,29]. In the same context, CuMn₂O₄, as a manganese-based ternary metal oxide, has shown potential photocatalytic characteristics for the removal of organic pollutants in wastewater [30,31]. In view of the above details, in this study, new ternary composites composed of pure and Sm-doped CuO/ZnO/CuMn₂O₄ were synthesized for efficient treatment of norfloxacin (antibiotic) and methyl green (dye) as examples of stable organic pollutants. The addition of an Sm dopant aims to reinforce the absorption of light energy and support the separation of the charge carriers. The synthesized ternary composites were characterized by different techniques and the photocatalytic activities were measured under free and natural sunlight energy. Furthermore, the electrical and dielectric performance of the samples were investigated and discussed. The obtained data confirmed that 98% of norfloxacin and 96% of methyl green were removed from contaminated water during 40–60 min for Sm-doped CuO/ZnO/CuMn₂O₄. Furthermore, Sm-doped CuO/ZnO/CuMn₂O₄ ternary composite has shown giant dielectric constant values, mainly at low frequencies, with low dielectric loss compared to a pure CuO/ZnO/CuMn₂O₄ composite.

2. Synthesis, Characterization, and Measurements

Pure and Sm-doped CuO/ZnO/CuMn₂O₄ ternary composites were prepared by using a co-precipitation approach. Firstly, CuO/CuMn₂O₄ powder was synthesized by dissolving 9.6 g Cu(NO₃)₂·3H₂O (Sigma Aldrich, St. Louis, MO, USA) and 4.9 g Mn(CH₃CO₂)₂·4H₂O (Sigma Aldrich) into 200 mL deionized water with continuous stirring for 30 min. NH₄OH solution was added drop by drop until pH was equal to 7.3 to form the precipitate. The obtained precipitate was deeply washed with deionized water until removing any dissolved impurities. Then, the acquired precipitate was dried and calcined at 650 °C to form CuO/CuMn₂O₄ binary composite with ratio of CuO to CuMn₂O₄ equal to 75:25%, respectively. After that, 1.35 g of Zn(CH₃CO₂)₂·2H₂O (Sigma Aldrich) was dissolved into 100 mL deionized water followed by addition of 2 g of the obtained CuO/CuMn₂O₄ binary composite with constant stirring for 45 min. Later, NH₄OH solution was added to precipitate the Zn ions in hydroxide form under continuous stirring. The obtained powder

was calcined at 500 °C to form CuO/ZnO/CuMn₂O₄ ternary composite. For Sm-doped CuO/ZnO/CuMn₂O₄ sample, 0.195 g Sm(NO₃)₃ substance was added during the synthesis of CuO/CuMn₂O₄ and 0.02 g was added to Zn(CH₃CO₂)₂·2H₂O solution followed by using the same steps for pure CuO/ZnO/CuMn₂O₄ sample. Figure 1 shows a schematic diagram for the synthesis method for CuO/ZnO/CuMn₂O₄ ternary composite. The synthesized powders were analyzed by different techniques using X-ray diffraction device (Bruker D8 Advance, $\lambda = 1.5406 \text{ \AA}$), transmission electron microscope (JEOL JEM-2100, Tokyo, Japan), scanning electron microscope (JSM-IT200, Tokyo, Japan), Brunauer–Emmett–Teller (BET) surface area (NOVA 3200, Davie, FL, USA), and UV–visible diffuse reflectance spectroscopy (Shimadzu UV-2050, Tokyo, Japan). The relations between frequency and dielectric or ac electrical conductivity of pure and Sm-doped CuO/ZnO/CuMn₂O₄ ternary composites were measured in pellet form (thickness = 2.5 mm and radius = 0.45 cm) at room temperature based on LCR device (Hioki 3532-50, Ha Noi City, Vietnam). The photocatalytic activity of pure and Sm-doped CuO/ZnO/CuMn₂O₄ ternary composites were established for elimination of norfloxacin and methyl green with concentration 15 mg/L as known examples for dissolved organic waste. The added catalyst dose to 100 mL solution of pollutant is 0.05 g. The mixed solution of the catalyst and dissolved pollutant was stirred under dark conditions and following that, irradiated by ordinary solar light energy. The average solar radiation was measured to be $\sim 780 \pm 10 \text{ W/m}^2$ (August, 12–2 pm). The variation of pollutant concentration was observed by measuring the absorbance (norfloxacin $\lambda_{\text{max}} = 278 \text{ nm}$ and methyl green $\lambda_{\text{max}} = 633 \text{ nm}$) of the solution at different times.

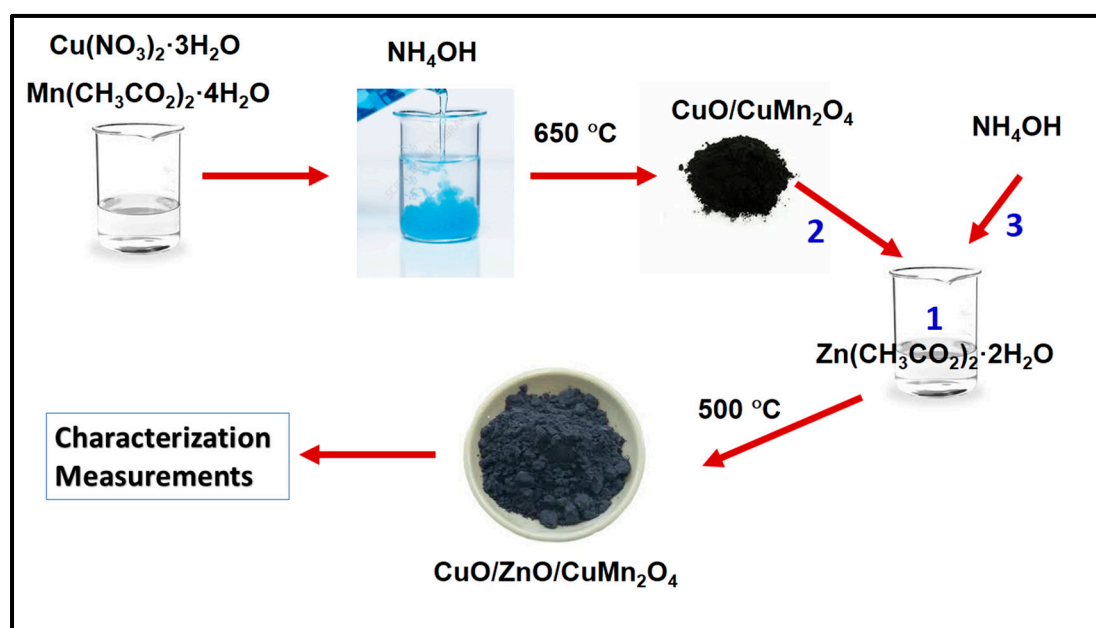


Figure 1. Schematic diagram of the synthesis method for CuO/ZnO/CuMn₂O₄ ternary composite.

3. Results and Discussion

3.1. XRD Investigation

The X-ray diffraction (XRD) technique is used to analyze the crystalline structures of synthesized powders. Figure 2 displays the XRD results of pure and Sm-doped CuO/ZnO/CuMn₂O₄ tri-composites. The X-ray diffraction pattern of the pure CuO/ZnO/CuMn₂O₄ tri-composite revealed various peaks with different relative intensities. In Figure 2, the peaks at 2-theta values of 32.55°, 35.54°, 38.72°, 48.65°, 53.51°, 58.12°, 61.45°, 65.99°, 67.8°, 72.2°, and 75.94° were related to (110) (11-1), (111), (20-2), (020), (202), (11-3), (022), (220), (311), and (22-2) crystallographic planes of CuO with monoclinic phase in agreement with JCPDS (# 48-1548, space group: C2/c). Additionally, the pattern also displayed another series of XRD peaks at $2\theta = 31.76^\circ, 34.38^\circ, 36.19^\circ, 47.46^\circ, 56.51^\circ, 62.70^\circ, 67.8^\circ, \text{ and } 68.99^\circ$,

recognized for (100), (002), (101), (102), (110), (103), (112), and (201) crystallographic planes of the zinc oxide phase with hexagonal structure (JCPDS. # 36-1451, space group: p63mc). The XRD peaks that appeared at 2-theta values of 18.74°, 30.31°, 35.54°, 43.8°, 57.72°, and 62.7° coincide with the crystallographic planes of (111), (220), (311), (400), (511), and (440) for cubic CuMn₂O₄ spinel oxide in agreement with JCPDS (# 74-1921 space group: Fd-3m). The Sm-doped CuO/ZnO/CuMn₂O₄ tri-composite has a similar XRD pattern to the pure one, which proves the same composite structure formation, Figure 2. The broadening of the X-ray diffraction peaks was improved after Sm ions doping which supports the reduction in the crystallite size. The Scherrer formula, as represented in Equation (1), was used to compute the average crystallite size of pure and Sm-doped CuO/ZnO/CuMn₂O₄ tri-composites through using the three main peaks of each phase [32]:

$$D = K\lambda / \beta \cos \theta \tag{1}$$

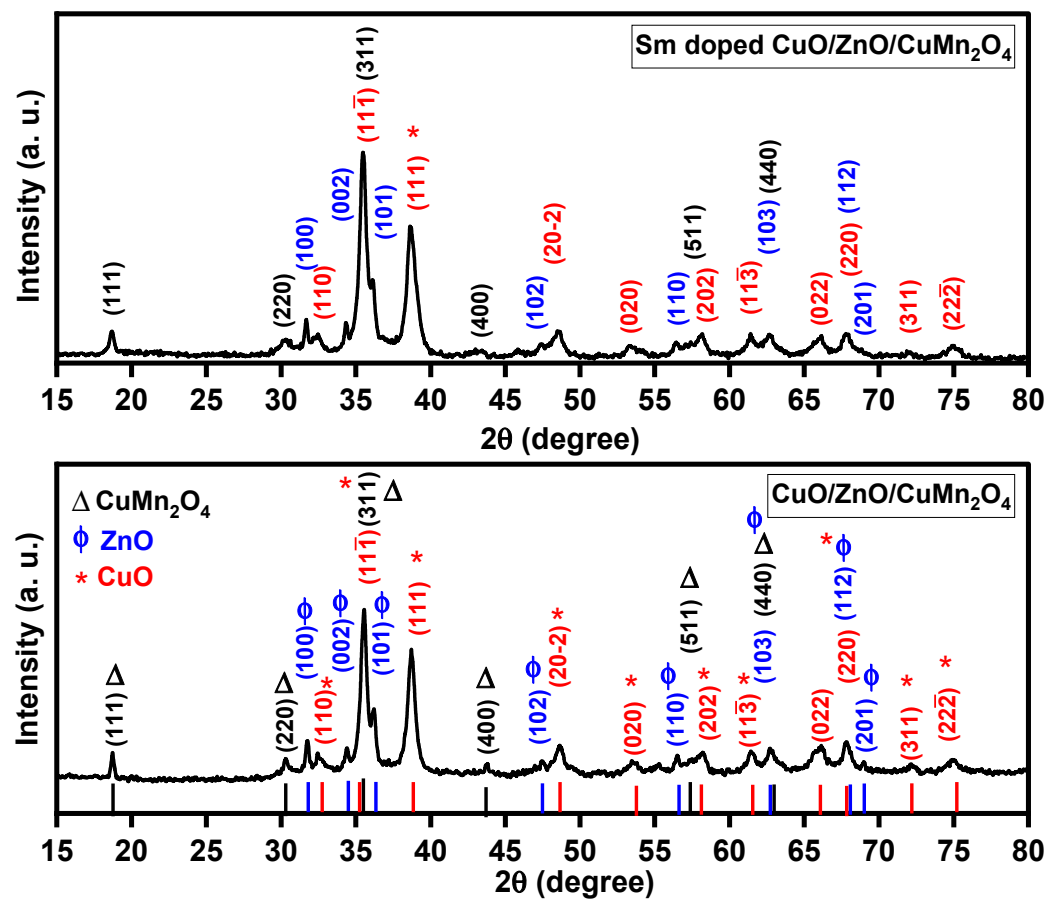


Figure 2. X-ray diffraction patterns of pure and “Sm-doped” CuO/ZnO/CuMn₂O₄ ternary composites.

In this formula, the θ , β , λ , K and D symbols are the Bragg angle, peak broadening at half the maximum (FWHM), wavelength of the used X-ray (1.5406 Å), dimensionless shape factor, and average crystallite size, respectively. For the pure composite, the D value was computed to be 29, 26, and 39 nm for CuO, ZnO, and CuMn₂O₄ phases, respectively. The average crystallite size of these constituents decreased to 23, 24, and 25 nm after Sm ions doping, respectively. The lattice constants of CuO, ZnO, and CuMn₂O₄ phases were computed by Rietveld refinement analysis based on Maud software (version 3.16.1.288) as tabulated in Table 1. As observed in Table 1, the lattice constants of CuO, ZnO, and CuMn₂O₄ were increased after doping by Sm ions. These expansions can be related to the substitution of Cu²⁺ (0.73 Å), Zn²⁺ (0.74 Å) and Mn³⁺ (0.58 Å) cations by Sm³⁺ (0.958 Å) ions of larger ionic radius.

Table 1. Calculated lattice constants (a, b, c) and unit cell volume (V) of CuO, ZnO and CuMn₂O₄ phases for both ternary composites.

Samples	Phase	a (Å)	b (Å)	c (Å)	V (Å ³)
CuO/ZnO/CuMn ₂ O ₄	CuO	4.696	3.426	5.135	81.51
	ZnO	3.254	3.254	5.219	47.89
	CuMn ₂ O ₄	8.343	8.343	8.343	580.8
Sm-CuO/ZnO/CuMn ₂ O ₄	CuO	4.702	3.428	5.140	81.69
	ZnO	3.262	3.262	5.224	48.14
	CuMn ₂ O ₄	8.350	8.350	8.350	582.2

3.2. Optical Properties: UV–Visible Diffuse Reflectance

Figure 3 depicts the UV–visible diffuse reflectance spectra of pure and Sm-doped CuO/ZnO/CuMn₂O₄ tri-composites. As shown in Figure 3, the reflectance spectra of both composites display three reduction regions of intensity (%), which related to the individual absorption edge of each phase including CuO, ZnO, and CuMn₂O₄ structures. It can be seen that these absorption edges were moved to a low energy direction after doping by Sm ions. This behavior signifies that the Sm-doped CuO/ZnO/CuMn₂O₄ tri-composite has a more harvesting of visible light spectrum compared to pure sample. As reported for metal oxides, perovskites, and composites materials, the formula of Tauc method can be used to compute the band gap energy of pure and Sm-doped CuO/ZnO/CuMn₂O₄ samples as shown in Equation (2) [33,34]:

$$\alpha = A (h\nu - E_g)^n / h\nu \tag{2}$$

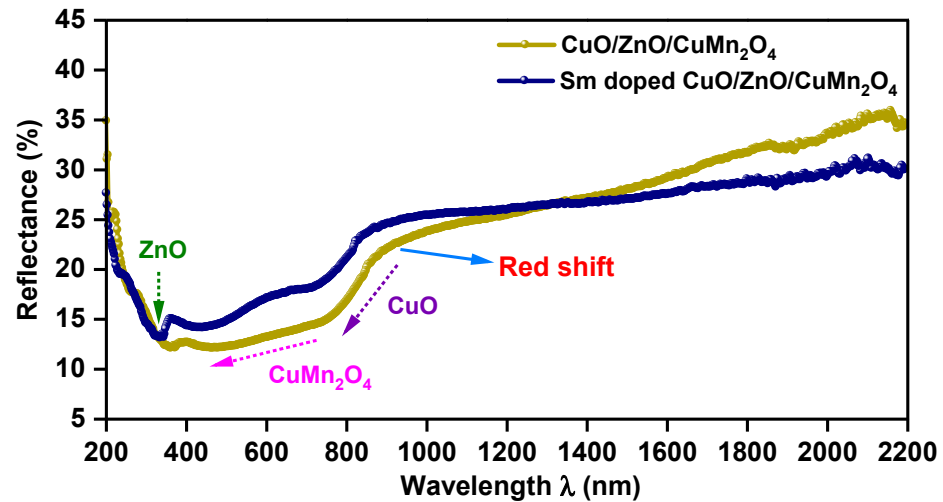


Figure 3. UV–visible diffuse reflectance (%) vs. wavelength (nm) for pure and Sm-doped CuO/ZnO/CuMn₂O₄ tri-composites.

In this formula, $h\nu$, n , E_g , A , and α are the energy of wavelength, constant, band gap energy, independent constant, and absorption coefficient, respectively. The Kubelka–Munk (K–M) formula is used to transform the reflectance spectra to absorption according to Equation (3) [33,34]:

$$F(R) = \frac{(1 - R)^2}{2R} = \frac{\alpha}{S} \tag{3}$$

where, S , R and $F(R)$ symbols are the scattering coefficient, reflectance, and the Kubelka–Munk function, respectively. As represented in Figure 4, the $[F(R) h\nu]^2$ was plotted opposed to energy of wavelength ($h\nu$) and the lengthening of the descending parts of the curves produce the exact band gap energies of pure and Sm-doped CuO/ZnO/CuMn₂O₄ samples. Three band gap energies were found for the pure CuO/ZnO/CuMn₂O₄ composite with

values of 1.45, 3.29, and 1.85 eV, which match with the energy gaps of ZnO, CuMn₂O₄, and CuO phases, respectively [35–37]. The doping by Sm ions induced red shifts of the band gap energies of ZnO, CuMn₂O₄, and CuO phases to 2.79, 1.66, and 1.43 eV, respectively. The insertion of Sm ions leads to broad absorption of visible light spectrum particularly for ZnO phase. The noticed decreases in the band gap energies support the replacement of Sm ions for Zn, Cu, or Mn sites into the CuO/ZnO/CuMn₂O₄ composite. This lessening in the band gap energies may be attributed to the transfer of the electrons between Sm 4f level and the conduction or valence band of ZnO, CuO, or CuMn₂O₄ [38]. Therefore, the doped composite could be a promising composition for photocatalytic applications, as it boosts the harvesting of visible light spectrum.

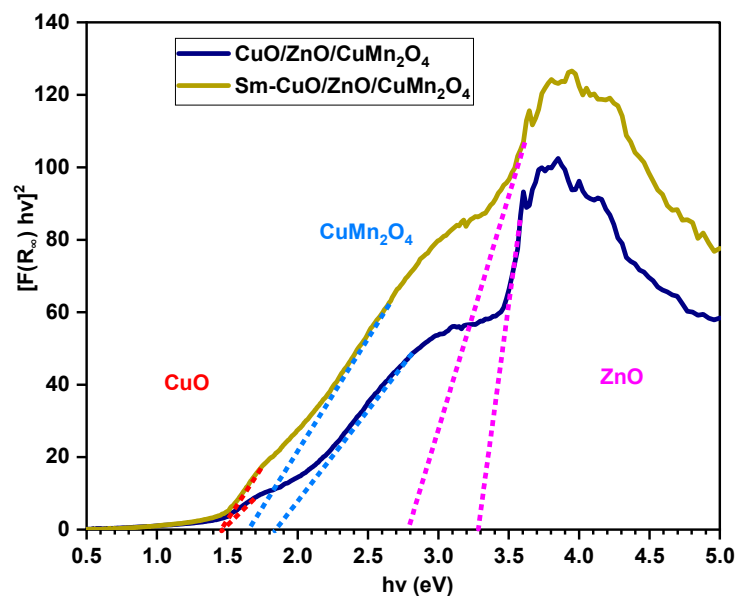


Figure 4. Estimation of band gap energies of pure and Sm-doped CuO/ZnO/CuMn₂O₄ tri-composites.

3.3. Morphology and Surface Area

The scanning electron microscope (SEM) micrographs of pure and Sm-doped CuO/ZnO/CuMn₂O₄ tri-composites are depicted in Figure 5. The images of both powders reveal the formation of semi-symmetrical spherical grains with finer structure in the case of the Sm-doped composite. Both samples have homogenous surface distribution with a certain degree of agglomeration. Figure 6 demonstrates the transmission electron microscope (TEM) images with corresponding particle size distribution histograms of the pure and Sm-doped CuO/ZnO/CuMn₂O₄ tri-composites. The TEM images display that the majority of the particles have a spherical shape with average mean size of 29 and 26 nm for the pure and Sm-doped CuO/ZnO/CuMn₂O₄ tri-composites, respectively. As presented in Figure 7, the compositional analysis based on energy dispersive X-ray technique confirms the presence of only Cu, Zn, Mn, and O elements in the pure CuO/ZnO/CuMn₂O₄ tri-composite. The EDX pattern of the doped composite reveals the existence of Cu, Zn, Mn, Sm, and O elements with measured wt% of Sm dopant equal to 2.23, which nearly match with the added value (3 wt%). No noticeable peaks related to any impure elements were detected, confirming the purity of the synthesized composites. Figure 8 depicts the nitrogen adsorption/desorption curves of the pure and Sm-doped CuO/ZnO/CuMn₂O₄ tri-composites, the plots inset in Figure 8 represent the pore size distribution. The pure CuO/ZnO/CuMn₂O₄ tri-composite has shown a BET surface area of 3.11 m²/g with total pore volume and pore size of 0.11 cm³/g and 7.8 nm, respectively. The BET surface area of the CuO/ZnO/CuMn₂O₄ tri-composite was improved to 4.24 m²/g after addition of Sm ions with measured total pore volume and pore size of 0.17 cm³/g and 10 nm, respectively.

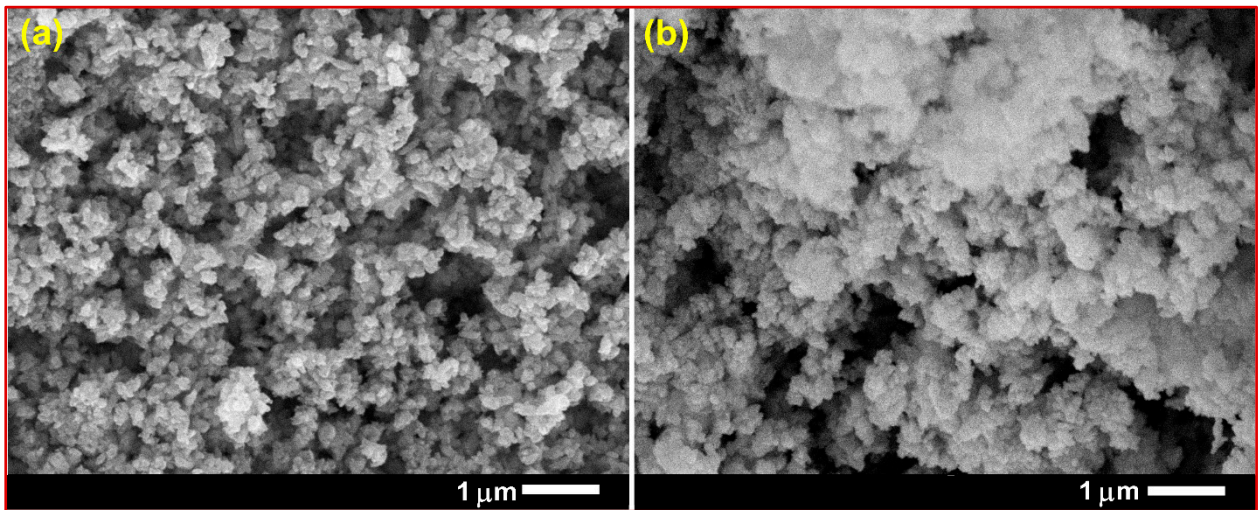


Figure 5. SEM images of (a) pure and (b) Sm-doped CuO/ZnO/CuMn₂O₄ tri-composites.

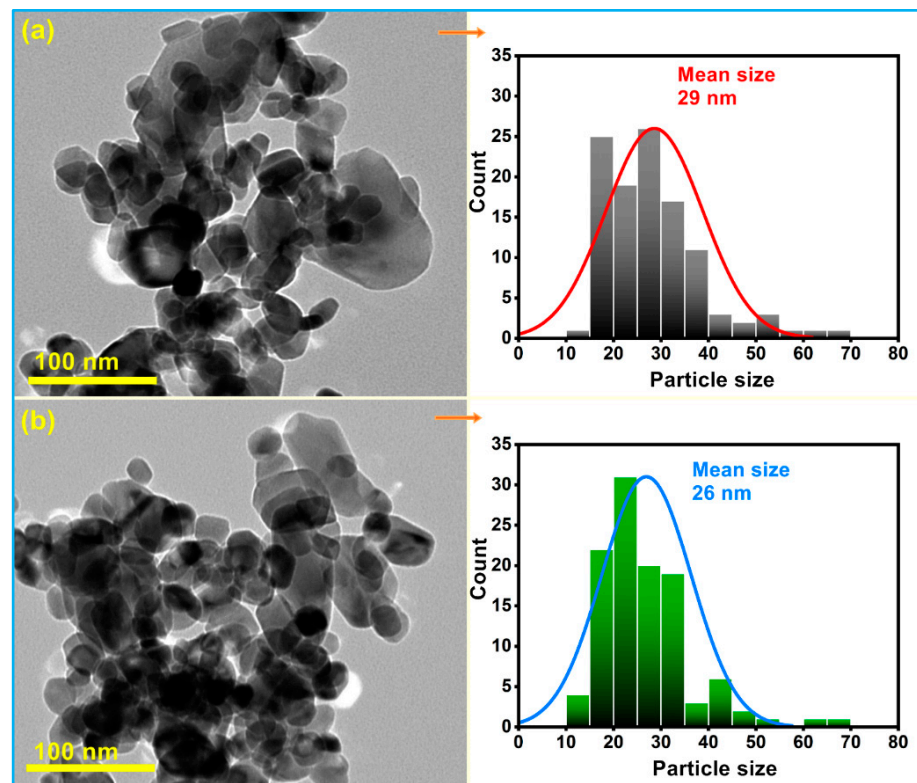


Figure 6. TEM images with corresponding particle size distribution histograms of (a) pure and (b) Sm-doped CuO/ZnO/CuMn₂O₄ tri-composites.

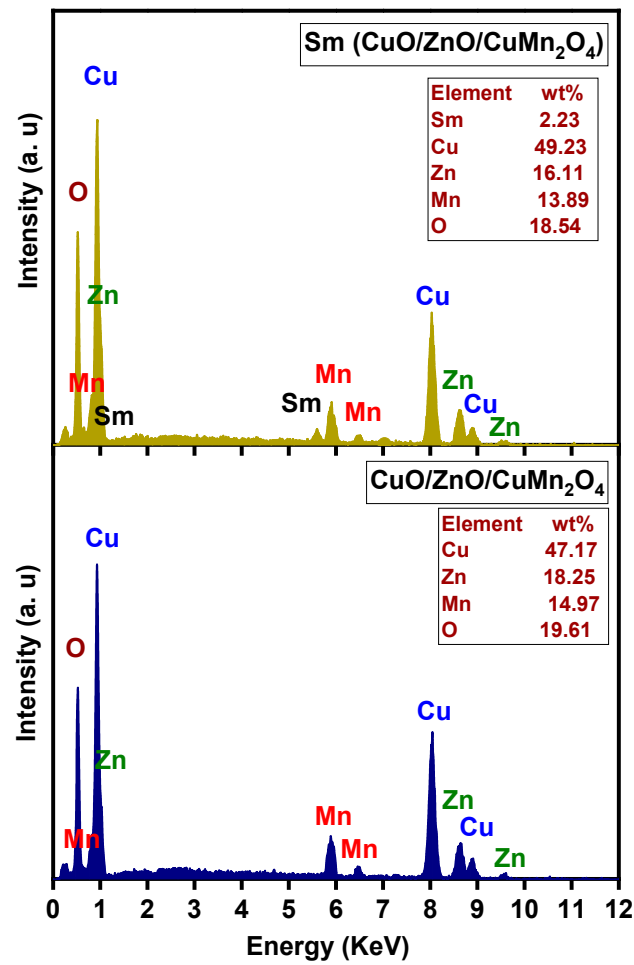


Figure 7. EDX patterns of pure and Sm-doped CuO/ZnO/CuMn₂O₄ tri-composites.

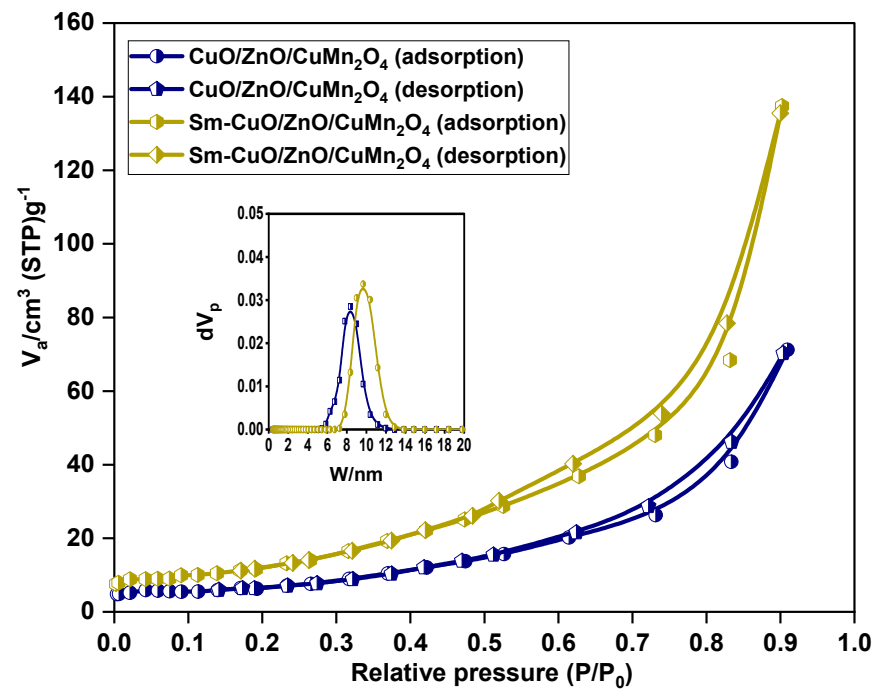


Figure 8. BET surface area of pure and Sm-doped CuO/ZnO/CuMn₂O₄ tri-composites, with inset pore size distribution.

3.4. Treatment of Dissolved Organic Waste

Figure 9 shows the time dependent UV–visible absorbance curve of 15 mg/L norfloxacin solution under dark stirring, and after exposure to solar light energy in the presence of pure and Sm-doped CuO/ZnO/CuMn₂O₄ tri-composites. The measured change in the UV–visible absorbance curve of norfloxacin solution reveals that the pure CuO/ZnO/CuMn₂O₄ catalyst has an adsorption capacity of 9% after 20 min of dark stirring. After exposed to solar light energy the absorbance curve of norfloxacin was decreased, with computed photodegradation efficiency of 67% after 50 min. In the case of the Sm-doped CuO/ZnO/CuMn₂O₄ tri-composite, the variation in the UV–visible absorbance of norfloxacin demonstrated that the adsorption capacity was 16% after 20 min of dark stirring while the degradation activity significantly increased to 97% after 50 min of solar illumination. The presence of Sm ions as a dopant activates the photodegradation process of the CuO/ZnO/CuMn₂O₄ tri-composite. The dependence of C_t/C₀ on the irradiation time of the pure and Sm-doped CuO/ZnO/CuMn₂O₄ tri-composites is illustrated in Figure 10a. The plotted curves show that the C_t/C₀ strongly and continuously decreases with increasing time of irradiation for the Sm-doped CuO/ZnO/CuMn₂O₄ catalyst. Furthermore, the kinetic performance and the apparent rate constant for the photocatalytic degradation of norfloxacin was quantitatively evaluated through fitting the obtained experimental values to the pseudo first-order rate equation [39]:

$$\ln\left(\frac{C_0}{C_t}\right) = kt \quad (4)$$

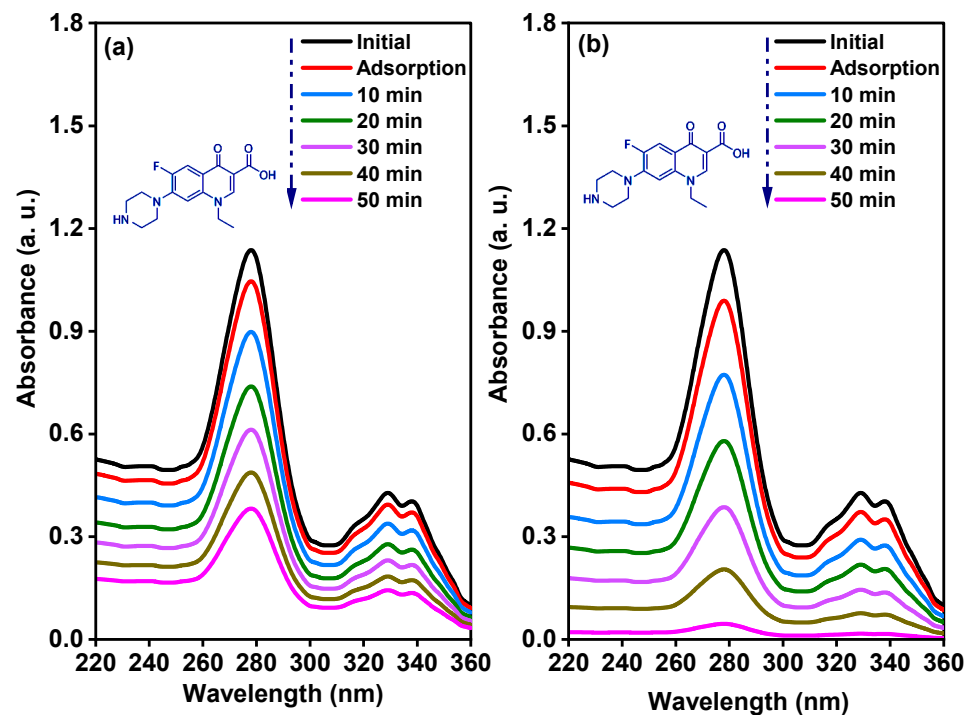


Figure 9. Time-dependent UV–visible absorption spectra of norfloxacin solution for (a) CuO/ZnO/CuMn₂O₄ and (b) Sm-doped CuO/ZnO/CuMn₂O₄ ternary composites.

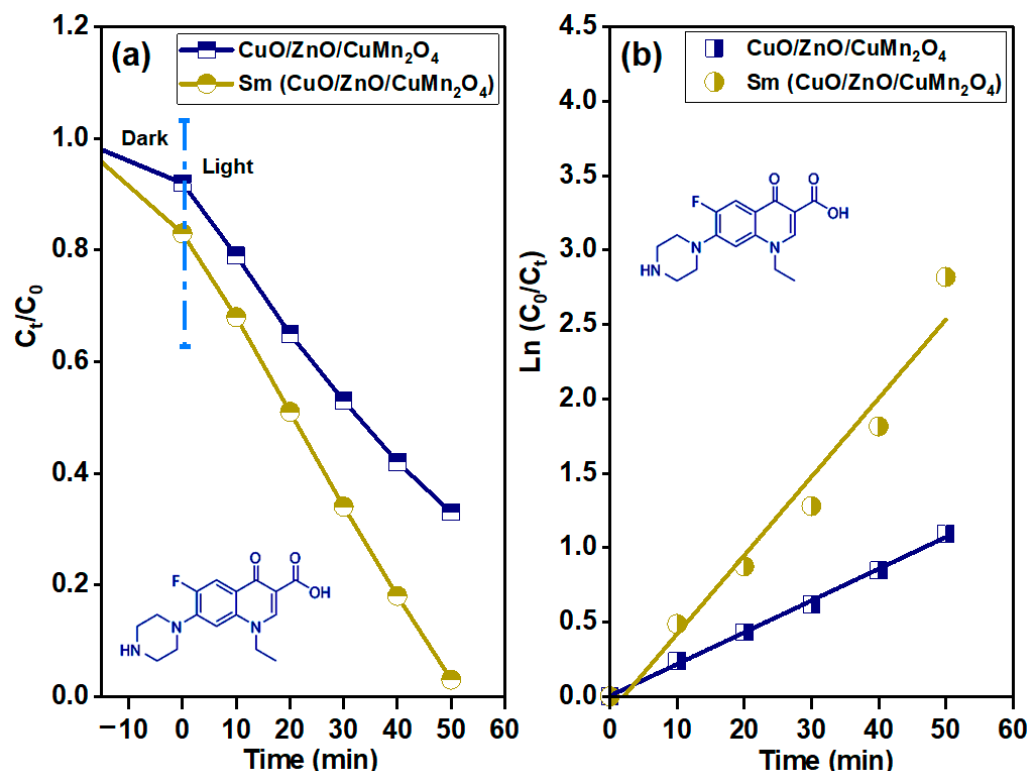


Figure 10. (a) C_t/C_0 with time plots and (b) variation of $\ln(C_0/C_t)$ with time to find the apparent rate constant for the degradation of norfloxacin antibiotic in the existence of pure and Sm-doped CuO/ZnO/CuMn₂O₄ ternary composites.

In this formulation, C_0 and C_t represent the concentration of the norfloxacin at time (t) = zero and at different irradiation times (min), respectively, while k signifies the apparent rate constant (min^{-1}) of the photodegradation reaction. Figure 10b shows the linear fitting relationship between $\ln(C_0/C_t)$ and the time (min) for both catalysts. Remarkably, the photodegradation apparent rate constant (k) of the Sm-doped CuO/ZnO/CuMn₂O₄ catalyst (0.053 min^{-1}) is significantly higher than that of the pure CuO/ZnO/CuMn₂O₄ tri-composite (0.021 min^{-1}).

Figure 11a,b displays the time dependent UV–visible absorbance spectra of 15 mg/L methyl green solution under dark stirring for 20 min and after exposure to solar energy for 40 min in the presence of pure and Sm-doped CuO/ZnO/CuMn₂O₄ tri-composites, respectively. The estimated change in the absorbance indicated that the adsorption and photodegradation values of the pure CuO/ZnO/CuMn₂O₄ catalyst towards methyl green dye were 8% and 70%, respectively. Interestingly, the Sm-doped CuO/ZnO/CuMn₂O₄ catalyst exhibits an adsorption value of 14% with a total degradation efficiency of 96% in 40 min towards 15 mg/L methyl green solution. As shown in Figure 11c, the change in C_t/C_0 with time reveals the fast removal of the dye for Sm-doped CuO/ZnO/CuMn₂O₄ compared to the pure catalyst. The kinetic study of the photodegradation reaction points out that the pure CuO/ZnO/CuMn₂O₄ catalyst has an apparent rate constant of 0.027 min^{-1} ($R^2 = 0.97$), whereas the Sm-doped CuO/ZnO/CuMn₂O₄ possesses an apparent rate constant of 0.067 min^{-1} ($R^2 = 0.95$), shown in Figure 11d. The remarkable degradation efficiency of the Sm-doped CuO/ZnO/CuMn₂O₄ ternary composite can be related to the synergistic effect of some factors. Optically, the Sm-doped CuO/ZnO/CuMn₂O₄ ternary composite shows higher harvesting for visible light energy compared to the pure composite, owing to the decreases in the band gap energies. The SEM and TEM images illustrated that the addition of Sm ions produces finer particles with a small nano-size. The BET surface area analysis proved that the Sm-doped CuO/ZnO/CuMn₂O₄ sample has a higher surface area when compared to pure powder, which consequently increases the active

surface sites for degradation of the organic molecules. Furthermore, Sm^{3+} ions can act as electron trapping states which hinder the recombination of the charge carriers (electron–hole pair) [40,41]. The reduced Sm^{2+} state may transfer the trapped electron to the oxygen molecule, leading to superoxide ($\cdot\text{O}_2^-$) formation. The remaining uncombined hole (h^+) interacts with a water (H_2O) molecule to form the hydroxyl ($\cdot\text{OH}$) radical. Both radicals are very important in degrading the organic molecules.

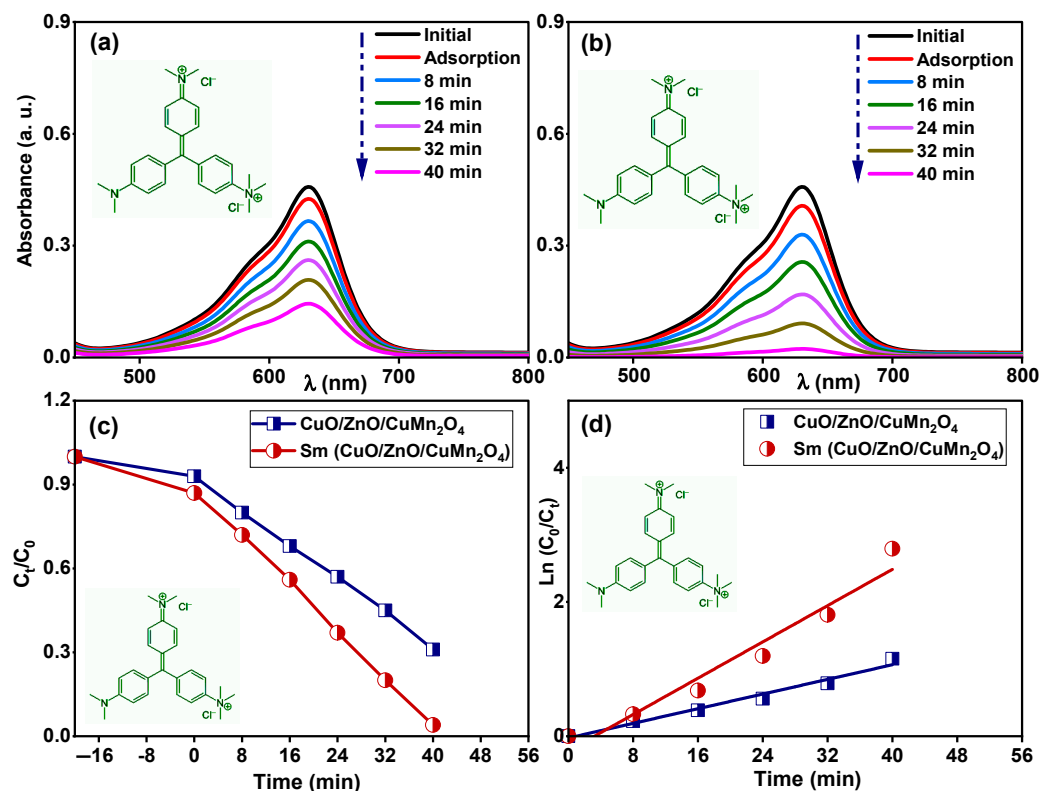


Figure 11. Time dependent UV–visible absorption spectra of 15 mg/L methyl green dye for (a) pure and (b) Sm-doped CuO/ZnO/CuMn₂O₄ catalysts, (c) C_t/C_0 with time, and (d) variation of $\ln(C_0/C_t)$ with time for both samples.

To examine the reactive species existing during the photocatalytic reaction using the Sm-doped CuO/ZnO/CuMn₂O₄ catalyst, the photocatalysis of norfloxacin and methyl green pollutants were investigated in the occurrence of reactive scavengers. The main reactive species produced by the Sm-doped CuO/ZnO/CuMn₂O₄ catalyst are considered to be hydroxyl radicals ($\cdot\text{OH}$), superoxide ($\cdot\text{O}_2^-$) radicals, electron (e^-), and hole (h^+) which can be scavenged by isopropyl alcohol (IPA), ascorbic acid (AsA), ethylenediaminetetraacetic acid (EDTA) and silver nitrate (AgNO_3), respectively. Figure 12a displays the reactive species scavenging photo-activity during the photodegradation reaction of norfloxacin and methyl green pollutants over the Sm-doped CuO/ZnO/CuMn₂O₄ catalyst. Upon the addition of the different scavengers to the photodegradation reaction, notable reductions in the norfloxacin and methyl green degradation were detected. Principally, the photodegradation efficiency of norfloxacin decreased from 97% to 46% by the addition of isopropyl alcohol, followed by 55% with the introduction of ascorbic acid. In addition, the isopropyl alcohol and ascorbic acid reduce the photocatalytic activity towards methyl green dye from 96% to 61 and 48%, respectively. These measured values indicate that the hydroxyl ($\cdot\text{OH}$) and superoxide ($\cdot\text{O}_2^-$) radicals play principle roles in the degradation of norfloxacin and methyl green pollutants. For a better understanding of the photodegradation mechanism, the total organic carbon (TOC) analysis was carried out to estimate the mineralization efficiency of norfloxacin and methyl green pollutants to CO_2 and H_2O in the presence of the Sm-doped CuO/ZnO/CuMn₂O₄ catalyst, as illustrated in Figures 12b and 12c, respectively. Mostly,

the mineralization of norfloxacin and methyl green pollutants happens in two steps. The primary step includes the ring opening of norfloxacin and methyl green molecules, which is followed by the successive oxidation of the produced fragments. Therefore, the mineralization process is expected to take more time than the decolorization process of norfloxacin and methyl green molecules in the presence of the Sm-doped CuO/ZnO/CuMn₂O₄ photocatalyst. The TOC results revealed that the mineralization percentages of both pollutants increased with time to reach 89 and 91% after 70 and 56 min, respectively.

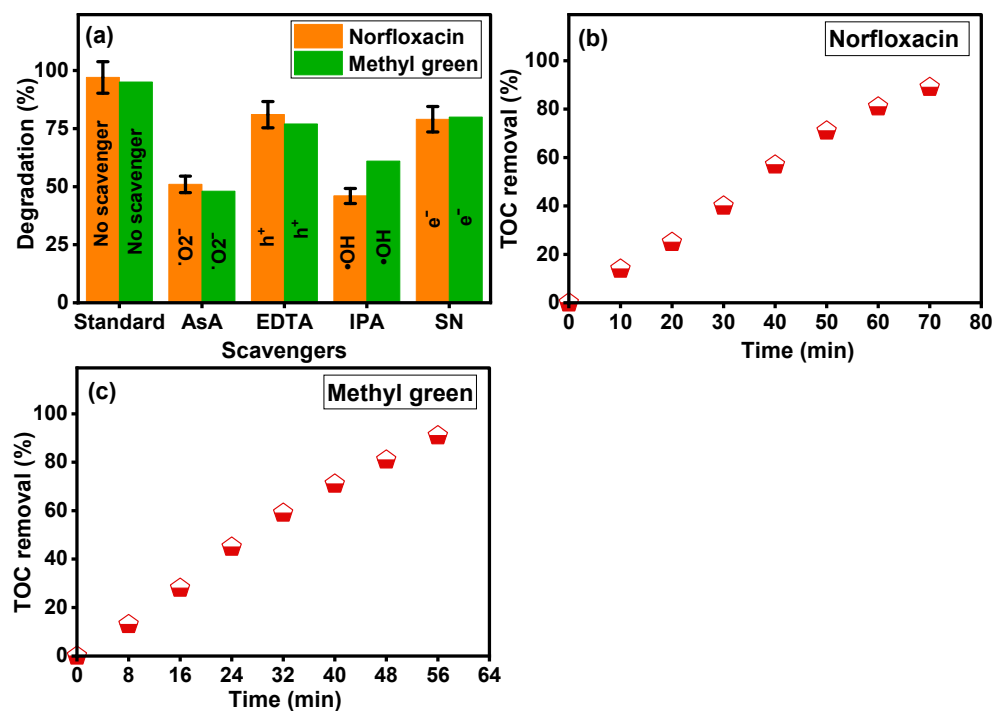


Figure 12. (a) Detection of main radicals by using different scavengers, (b) TOC analysis for norfloxacin, and (c) TOC analysis for methyl green dye of Sm-doped CuO/ZnO/CuMn₂O₄ catalyst.

The stability of the catalyst after several uses is an essential factor for the actual photocatalytic applications. Figure 13a,b shows the obtained results for the photodegradation reaction of the Sm-doped CuO/ZnO/CuMn₂O₄ photocatalyst for three cycles against norfloxacin and methyl green pollutants, respectively. The measured reusability efficiency indicated that the Sm-doped CuO/ZnO/CuMn₂O₄ photocatalyst has a photodegradation value of 97, 90, and 84% for the norfloxacin compound while for methyl green, the activity was estimated to be 96, 91, and 87% during the three cycles, respectively. The integration factors point out that the Sm-doped CuO/ZnO/CuMn₂O₄ ternary composite is a promising photocatalyst for the removal of organic pollutants with high mineralization efficiency and stability. The obtained results for the photodegradation properties of Sm-doped CuO/ZnO/CuMn₂O₄ photocatalyst were compared with previously published studies as reported in Table 2. The comparison reflects the high efficiency of the Sm-doped CuO/ZnO/CuMn₂O₄ photocatalyst towards organic pollutants degradation. As shown in Figure 14, the complete mechanistic picture of the photodegradation reaction of norfloxacin and methyl green molecules in the presence of the Sm-doped CuO/ZnO/CuMn₂O₄ photocatalyst under sunlight radiation can be explained based on scavenger tests and total organic carbon analysis. When Sm-doped CuO/ZnO/CuMn₂O₄ particles are exposed to solar light energy, electron-excitation happens, leading to the production of an electron-hole pair (e^- - h^+) as photoexcited charge carriers. The charge separation takes place between the different components through transfer of the electron from the p-type CuO to n-type ZnO or CuMn₂O₄, while the holes transfer in the opposite direction. Then, the h^+ and e^- interact with the water (H₂O) and oxygen (O₂) molecules to form \cdot OH and \cdot O₂⁻ radicals,

respectively [42,43]. Both OH and $\cdot\text{O}_2^-$ radicals attack the norfloxacin and methyl green molecules and mineralize them as shown below:

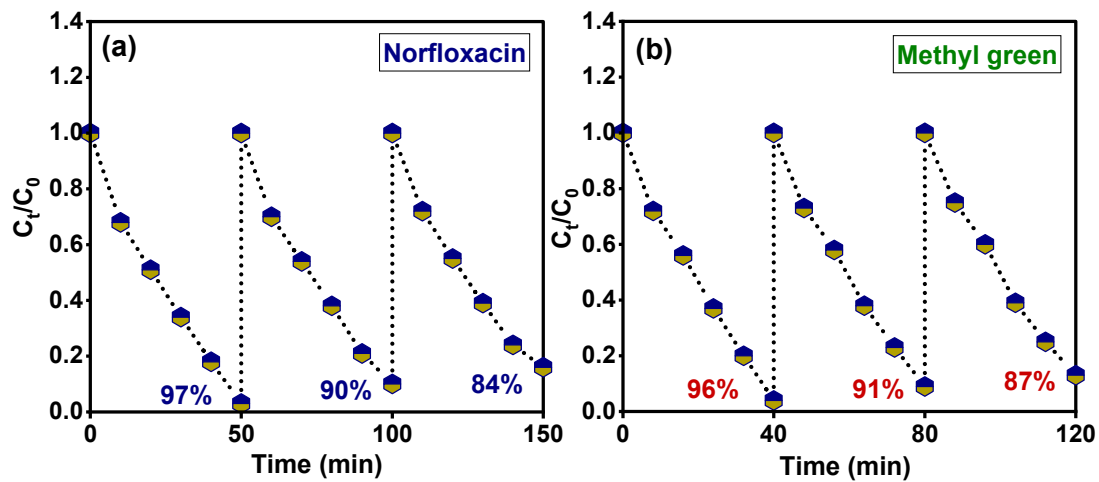
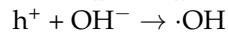
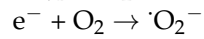
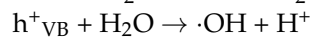
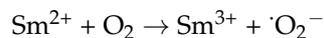
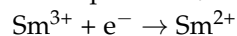
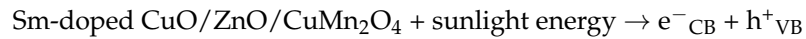


Figure 13. Reusability of Sm-doped CuO/ZnO/CuMn₂O₄ catalyst for (a) norfloxacin and (b) methyl green dye.

Table 2. Comparison of the obtained photocatalytic results with previously published studies.

Samples	Pollutant	Time (min)	Efficiency (%)	Reference
Sm-CuO/ZnO/CuMn ₂ O ₄	Norfloxacin	50	97	Current study
	Methyl green	40	96	
ZnO	Methylene blue	80	91	[44]
	Methyl orange	150	86	
2%Fe-ZnO	Methylene blue	180	92	[45]
CuO	Methyl green	60	65	[46]
	Methyl orange	60	65	
ZnO/CuO	Rhodamine B	180	98	[47]
Zn-CuO	Methylene blue	60	63	[48]
CuMn ₂ O ₄ /CuO	Malachite green	90	73.27	[49]
CuMn ₂ O ₄	Methylene Blue	120	86	[31]
	Malachite green	60	92	
ZnO/CuO	Methylene Blue	120	97.2	[50]
	Methyl orange	120	87.7	
CuO/ZnO	Rhodamine B	240	93	[51]

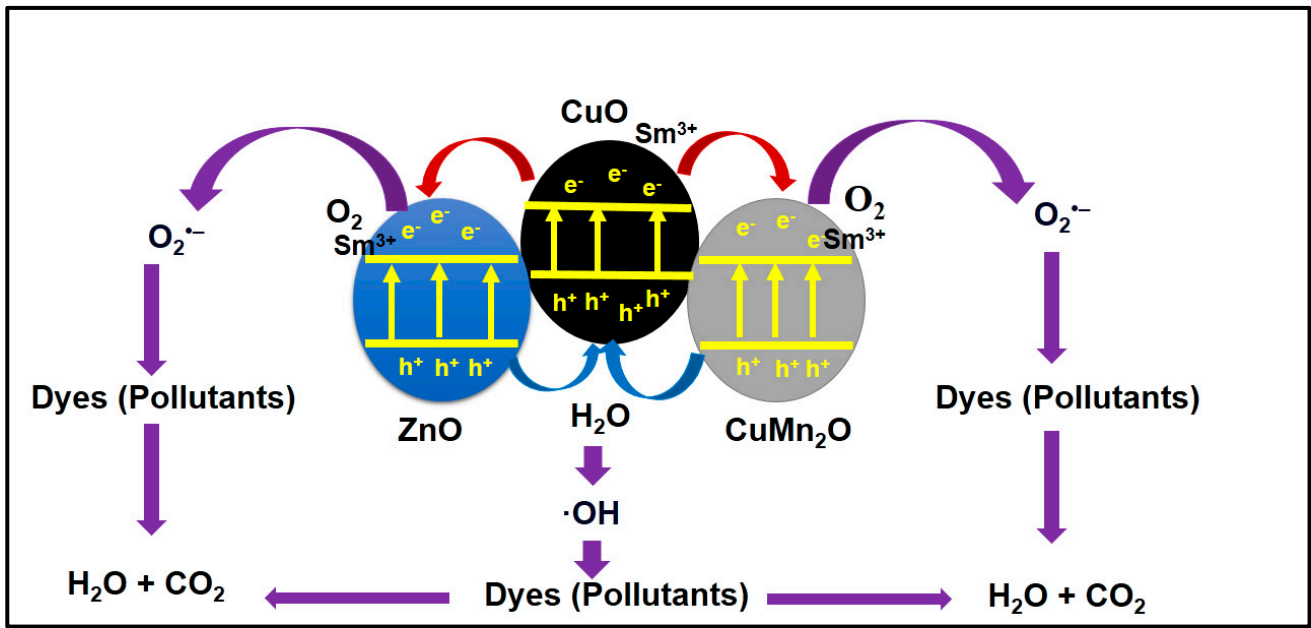


Figure 14. Proposed photocatalytic mechanism of Sm-doped CuO/ZnO/CuMn₂O₄ catalyst for removal of norfloxacin and methyl green dye.

3.5. Analysis of Ac Electrical Conductivity and Dielectric Properties

Figure 15a–c show the impact of changes in the applied frequency on the ac electrical conductivity, dielectric constant, and dielectric loss of pure and Sm-doped CuO/ZnO/CuMn₂O₄ tri-composites. As shown in Figure 15a, the trend of the ac electrical conductivity displays an increasing performance with growth in the applied frequency, particularly at higher frequencies, owing to the migration improvement of the charge carriers (electrons). At lower and middle frequencies (10²–10⁴ Hz), it can be seen that the improvement of the electrical conductivity is weak, and after that, it becomes very sharp at appropriately higher frequencies, especially for the Sm-doped CuO/ZnO/CuMn₂O₄ sample. As the frequency increases, the ac electrical conductivity of pure and Sm-doped CuO/ZnO/CuMn₂O₄ tri-composites becomes more frequency dependent. The applied frequency where the dispersion takes place is recognized as the hopping or critical frequency. It can be observed that the hopping or critical frequency moved towards a low frequency direction, owing to Sm ions doping into the CuO/ZnO/CuMn₂O₄ composite. This change in the electrical conductivity from the region of frequency-independent to the region of frequency-dependent emphasizes the electrical conductivity relaxation phenomenon [52,53]. The incorporation of Sm ions greatly enhances the ac electrical conductivity of the pure CuO/ZnO/CuMn₂O₄ ternary composite, especially at high frequencies. The performance may be attributed to the rise in the hopping process of charges between Sm³⁺ and Sm³⁺, which dominated over the charge carriers' blocking influence [51–54]. The optical characteristics indicated that the band gap energy of the composite components was reduced after insertion of Sm ions. In terms of Maxwell–Wagner interfacial theory [52], the regular growth of the ac electrical conductivity with the applied frequency can be understood. The grain boundaries, or the interfaces between grains, induce a potential barrier which restricts the movement of the charge carriers, resembling particles in a box [52]. The insignificant increases in the electrical conductivity at the low frequency domain can be related to the limited amount of charge carriers that can cross over this potential barrier, leading to weak ac electrical conductivity. Once the applied frequency is increased, the charge carriers acquire appropriate energy to move over the potential barrier, which was reflected in the quick improvements of the ac electrical conductivity at a higher frequency field.

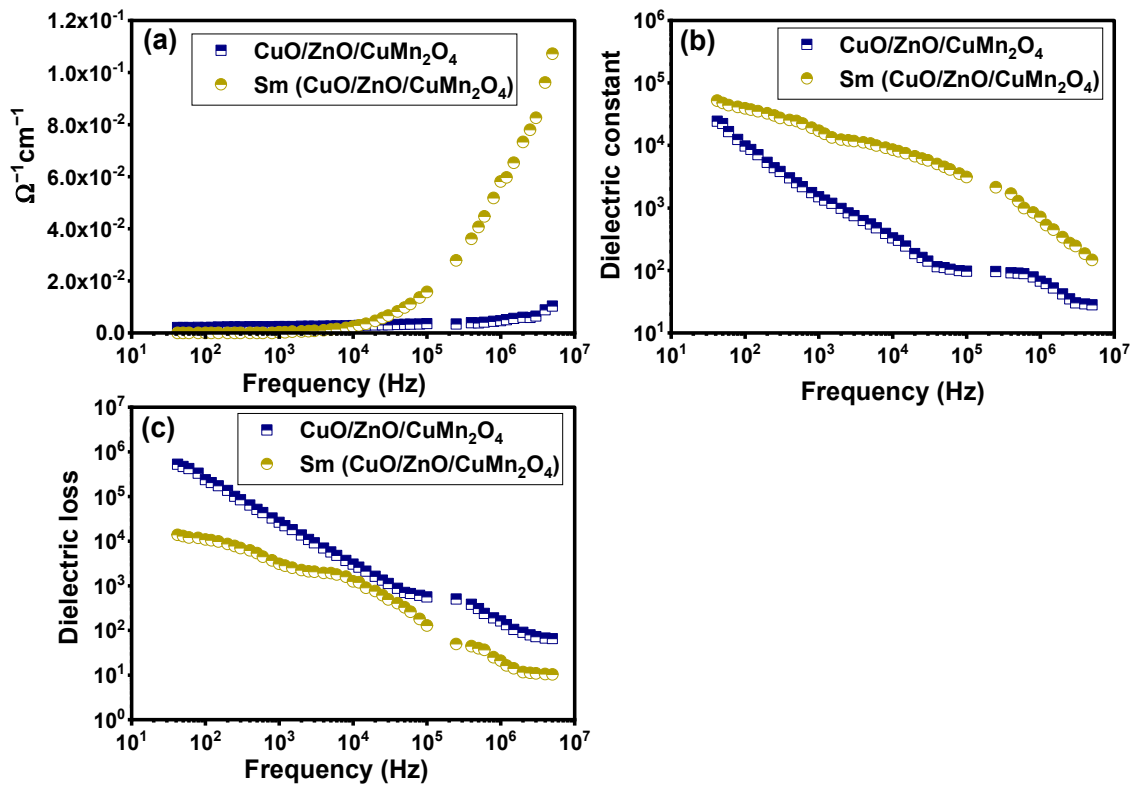


Figure 15. Dependency of (a) ac electrical conductivity, (b) dielectric constant, and (c) dielectric loss on frequency for pure and Sm-doped CuO/ZnO/CuMn₂O₄ ternary composites.

Figure 15b depicts the relationship between the dielectric constant (relative permittivity) and the applied frequency at room temperature for the pure and Sm-doped CuO/ZnO/CuMn₂O₄ ternary composites. The dielectric constant values of the pure CuO/ZnO/CuMn₂O₄ tri-composite was decreased significantly with increasing the frequency up to 10⁴ Hz. Above this frequency, the dielectric constant changed slowly or nearly remained constant. The performance of the dielectric constant after addition of Sm ions was greatly boosted. The values of the dielectric constant increased and became more stable at a lower frequency compared to the pure sample. At low and middle frequencies, the dielectric constant slowly decreased, and at higher frequency, the drop was high. Table 3 compares the dielectric constant values of the pure and Sm-doped CuO/ZnO/CuMn₂O₄ ternary composites at several frequencies. The reported results indicate that the Sm-doped CuO/ZnO/CuMn₂O₄ sample has colossal relative permittivity values (>10³) at many frequencies. Generally, such behavior of the dielectric dispersion in metal oxides or composites structures can be illuminated in the interpretation of Maxwell–Wagner interfacial theory, which is in agreement with Koops phenomenological philosophy [52,55]. In this explanation, the grains are highly conductive and become disjointed by grain boundaries, which are very poorly conductive. As a result, under an applied electric field, the charge carriers (electrons) are being collected or accumulated at the weak conducting grain boundaries or interfaces [52,55]. At the lower frequencies, the collection or the accumulation of the charge carriers at the high resistance grain boundaries includes a big polarizability, yielding a large polarization which is measured as a high dielectric constant value. Figure 15c displays the dependence of the dielectric loss on the applied frequency for pure and Sm-doped CuO/ZnO/CuMn₂O₄ ternary composites. These curves illustrate a high dielectric loss value for lower frequencies, and after that, it reduces to nearly stable values for higher frequencies. Interestingly, it can be seen that the incorporation of Sm ions into the CuO/ZnO/CuMn₂O₄ tri-composite reduces the dielectric loss which is a beneficial performance for energy storage applications. The observed high values of the dielectric loss

at low frequency can be related to impurities, defects in crystal lattice, and the adsorbed moisture in the tri-composite samples [52]. The drop in dielectric loss with the rise in the applied frequency can be understood based on domain wall resonance. Actually, at low frequencies, an extra energy is required for the motion of the charge carriers (electrons), owing to the high resistance of the grain boundary (interface), while the motion of the charge carriers requires less energy at higher frequencies due to the low resistance.

Table 3. Compare the dielectric constant values of pure and Sm-doped CuO/ZnO/CuMn₂O₄ ternary composites at several frequencies from 50 to 10,000 Hz.

Samples	50 Hz	100	250	500	1000	3000	5000	8000	10,000
CuO/ZnO/CuMn ₂ O ₄	22,448	9756	4383	2532	1507	749	556	390	332
Sm-CuO/ZnO/CuMn ₂ O ₄	47,845	39,254	30,214	24,562	17,211	11,726	10,709	9197	8579

4. Conclusions

In this work, pure and Sm-doped CuO/ZnO/CuMn₂O₄ ternary composites were successfully synthesized using the co-precipitation approach. The influence of Sm dopant on the optical, dielectric, electrical, and photocatalytic properties of the CuO/ZnO/CuMn₂O₄ ternary composite was studied and discussed. The XRD patterns verified the presence of CuO, ZnO, and CuMn₂O₄ constituents in the composite structure. The SEM and TEM images of the pure and Sm-doped CuO/ZnO/CuMn₂O₄ powder show the formation of homogenous spherical particles with a small size within 26–29 nm. The optical absorption analysis demonstrates that Sm doping of the CuO/ZnO/CuMn₂O₄ tri-composite greatly reinforces the harvesting of visible light energy compared to pure sample. The photocatalytic measurements for the removal of organic waste revealed that the Sm-doped CuO/ZnO/CuMn₂O₄ catalyst has photodegradation efficiencies of 97% for norfloxacin and 96% for methyl green. The reusability experiments confirmed the good stability of the Sm-doped CuO/ZnO/CuMn₂O₄ catalyst, along with a high mineralization efficiency to convert norfloxacin and methyl green molecules to carbon dioxide and water. For energy storage, Sm-doped CuO/ZnO/CuMn₂O₄ pellets exhibited a giant dielectric constant, principally at low frequency, with low dielectric loss values compared to the pure CuO/ZnO/CuMn₂O₄ sample.

Author Contributions: Conceptualization, methodology, software, validation, formal analysis, investigation, resources, data curation, writing—original draft preparation, writing—review and editing, visualization, supervision, project administration, funding acquisition were done by all authors with equal contributions. All authors have read and agreed to the published version of the manuscript.

Funding: The authors extend their appreciation to the Deanship of Scientific Research & Innovation, ministry of education in Saudi Arabia for funding this research work through the Project Number (INST211).

Data Availability Statement: The data presented in this study are available in this article.

Conflicts of Interest: The authors declare no conflict of interest.

References

1. Yue, C.; Chen, L.; Zhang, H.; Huang, J.; Jiang, H.; Li, H.; Yang, S. Metal–organic framework-based materials: Emerging high-efficiency catalysts for the heterogeneous photocatalytic degradation of pollutants in water. *Environ. Sci. Water Res. Technol.* **2023**, *9*, 669–695. [[CrossRef](#)]
2. Bano, K.; Kaushal, S.; Singh, P.P. A review on photocatalytic degradation of hazardous pesticides using heterojunctions. *Polyhedron* **2021**, *209*, 115465. [[CrossRef](#)]
3. Lee, D.-E.; Kim, M.-K.; Danish, M.; Jo, W.-K. State-of-the-art review on photocatalysis for efficient wastewater treatment: Attractive approach in photocatalyst design and parameters affecting the photocatalytic degradation. *Catal. Commun.* **2023**, *183*, 106764. [[CrossRef](#)]

4. Ahmad, A.; Mohd-Setapar, S.H.; Chuong, C.S.; Khatoon, A.; Wani, W.A.; Kumar, R.; Rafatullah, M. Recent advances in new generation dye removal technologies: Novel search for approaches to reprocess wastewater. *RSC Adv.* **2015**, *5*, 30801–30818. [[CrossRef](#)]
5. Waheed, A.; Baig, N.; Ullah, N.; Falath, W. Removal of hazardous dyes, toxic metal ions and organic pollutants from wastewater by using porous hyper-cross-linked polymeric materials: A review of recent advances. *J. Environ. Manag.* **2021**, *287*, 112360. [[CrossRef](#)] [[PubMed](#)]
6. Rajamani, M.; Rajan, A.; Neppolian, B. Photocatalytic pathway toward real time control of tetracycline from industrial wastewater mediated by hetero-structure $\text{CuFe}_2\text{O}_4\text{-SnS}_2$. *J. Environ. Chem. Eng.* **2023**, *11*, 109129. [[CrossRef](#)]
7. Jabbar, Z.H.; Graimed, B.H.; Alsunbuli, M.M.; Sabit, D.A. Developing a magnetic bismuth-based quaternary semiconductor boosted by plasmonic action for photocatalytic detoxification of Cr(VI) and norfloxacin antibiotic under simulated solar irradiation: Synergistic work and radical mechanism. *J. Alloys Compd.* **2023**, *958*, 170521. [[CrossRef](#)]
8. Nie, L.; Li, S.; Gao, X.; Yuan, S.; Dong, G.; Tang, G.; Song, D.; Bu, L.; Zhou, Q. Sensitive visual detection of norfloxacin in water by smartphone assisted colorimetric method based on peroxidase-like active cobalt-doped Fe_3O_4 nanozyme. *J. Environ. Sci.* **2025**, *148*, 198–209. [[CrossRef](#)]
9. Ghosh, S.; Kar, S.; Pal, T.; Ghosh, S. Sunlight-driven photocatalytic degradation of Norfloxacin antibiotic in wastewater by ZnSe microsphere functionalized RGO composite. *Sustain. Chem. Environ.* **2023**, *4*, 100038. [[CrossRef](#)]
10. Liu, R.; Guo, J.; Gan, W.; Chen, R.; Ding, S.; Zhao, Z.; Li, J.; Zhang, M.; Sun, Z. Construction of ZnCdS/TiO_2 Z-Scheme heterostructure with excellent photocatalytic performance for degradation of norfloxacin. *Appl. Surf. Sci.* **2024**, *650*, 159229. [[CrossRef](#)]
11. Zhu, Z.; Xia, H.; Ren, B.; Han, S.; Li, H. Fabrication of solar-driven $\text{Zn}_2\text{SnO}_4/\text{g-C}_3\text{N}_4$ photocatalyst with enhanced photocatalytic performance for norfloxacin. *Inorg. Chem. Commun.* **2023**, *149*, 110432. [[CrossRef](#)]
12. Geldasa, F.T.; Kebede, M.A.; Shura, M.W.; Hone, F.G. Experimental and computational study of metal oxide nanoparticles for the photocatalytic degradation of organic pollutants: A review. *RSC Adv.* **2023**, *13*, 18404–18442. [[CrossRef](#)] [[PubMed](#)]
13. Sandhu, Z.A.; Raza, M.A.; Farwa, U.; Nasr, S.; Yahia, I.S.; Fatima, S.; Munawar, M.; Hadayet, Y.; Ashraf, S.; Ashraf, H. Response surface methodology: A powerful tool for optimizing the synthesis of metal sulfide nanoparticles for dye degradation. *Mater. Adv.* **2023**, *4*, 5094–5125. [[CrossRef](#)]
14. Al-Tohamy, R.; Ali, S.S.; Li, F.; Okasha, K.M.; Mahmoud, Y.A.-G.; Elsamahy, T.; Jiao, H.; Fu, Y.; Sun, J. A critical review on the treatment of dye-containing wastewater: Ecotoxicological and health concerns of textile dyes and possible remediation approaches for environmental safety. *Ecotoxicol. Environ. Saf.* **2022**, *231*, 113160. [[CrossRef](#)]
15. Shabir, M.; Yasin, M.; Hussain, M.; Shafiq, I.; Akhter, P.; Nizami, A.-S.; Jeon, B.-H.; Park, Y.-K. A review on recent advances in the treatment of dye-polluted wastewater. *J. Ind. Eng. Chem.* **2022**, *112*, 1–19. [[CrossRef](#)]
16. Kumari, H.; Sonia; Suman; Ranga, R.; Chahal, S.; Devi, S.; Sharma, S.; Kumar, S.; Kumar, P.; Kumar, S.; et al. A Review on photocatalysis used for wastewater treatment: Dye degradation. *Water Air Soil Pollut.* **2023**, *234*, 349. [[CrossRef](#)] [[PubMed](#)]
17. Rafiq, A.; Ikram, M.; Ali, S.; Niaz, F.; Khan, M.; Khan, Q.; Maqbool, M. Photocatalytic degradation of dyes using semiconductor photocatalysts to clean industrial water pollution. *J. Ind. Eng. Chem.* **2021**, *97*, 111–128. [[CrossRef](#)]
18. Rouibah, K.; Akika, F.-Z.; Rouibah, C.; Boudermine, H.R.; Douafer, S.; Boukerche, S.; Boukerche, G.; Benamira, M. Solar photocatalytic degradation of Methyl green on $\text{CuFe}_2\text{O}_4/\alpha\text{-Fe}_2\text{O}_3$ heterojunction. *Inorg. Chem. Commun.* **2023**, *148*, 110361. [[CrossRef](#)]
19. Mosleh, S.; Dashtian, K.; Ghaedi, M.; Amiri, M. A $\text{Bi}_2\text{WO}_6/\text{Ag}_2\text{S}/\text{ZnS}$ Z-scheme heterojunction photocatalyst with enhanced visible-light photoactivity towards the degradation of multiple dye pollutants. *RSC Adv.* **2019**, *9*, 30100–30111. [[CrossRef](#)]
20. Liu, D.; Cai, H.; Zhou, W.; Lei, D.; Cao, C.; Xia, X.; Xiao, L.; Qian, Q.; Chen, Q. Application of 3D printing technology for green synthesis of Fe_2O_3 using ABS/TPU/chlorella skeletons for methyl orange removal. *RSC Adv.* **2024**, *14*, 1501–1512. [[CrossRef](#)]
21. Ismael, A.M.; El-Shazly, A.N.; Gaber, S.E.; Rashad, M.M.; Kamel, A.H.; Hassan, S.S.M. Novel $\text{TiO}_2/\text{GO}/\text{CuFe}_2\text{O}_4$ nanocomposite: A magnetic, reusable and visible-light-driven photocatalyst for efficient photocatalytic removal of chlorinated pesticides from wastewater. *RSC Adv.* **2020**, *10*, 34806–34814. [[CrossRef](#)] [[PubMed](#)]
22. Perumal, K.; Shanavas, S.; Ahamad, T.; Karthigeyan, A.; Murugakoothan, P. Construction of $\text{Ag}_2\text{CO}_3/\text{BiOBr}/\text{CdS}$ ternary composite photocatalyst with improved visible-light photocatalytic activity on tetracycline molecule degradation. *J. Environ. Sci.* **2023**, *125*, 47–60. [[CrossRef](#)] [[PubMed](#)]
23. Bai, Y.; Zhang, S.; Feng, S.; Zhu, M.; Ma, S. The first ternary Nd-MOF/GO/ Fe_3O_4 nanocomposite exhibiting an excellent photocatalytic performance for dye degradation. *Dalton Trans.* **2020**, *49*, 10745–10754. [[CrossRef](#)]
24. Kighuta, K.; Gopalan, A.-I.; Lee, D.-G.; Kim, S.-W.; Park, S.-S.; Lee, D.-E.; Lee, K.-P.; Kim, W.-J. Novel visible light active ternary $\text{TiO}_2\text{-ZnO-WO}_3$ composites: Facile preparation strategy and performance evaluation using the response surface design. *J. Environ. Chem. Eng.* **2022**, *10*, 108224. [[CrossRef](#)]
25. Ali, H.R.; Motawea, E.A. Ternary photodegradable nanocomposite ($\text{BiOBr}/\text{ZnO}/\text{WO}_3$) for the degradation of phenol pollutants: Optimization and experimental design. *ACS Omega* **2021**, *6*, 22047–22064. [[CrossRef](#)]
26. Wu, Z.; Chen, X.; Liu, X.; Yang, X.; Yang, Y. A ternary magnetic recyclable $\text{ZnO}/\text{Fe}_3\text{O}_4/\text{g-C}_3\text{N}_4$ composite photocatalyst for efficient photodegradation of Monoazo dye. *Nanoscale Res. Lett.* **2019**, *14*, 147. [[CrossRef](#)] [[PubMed](#)]
27. Liu, H.; Hu, C.; Zhai, H.; Yang, J.; Liu, X.; Jia, H. Fabrication of $\text{In}_2\text{O}_3/\text{ZnO}@\text{Ag}$ nanowire ternary composites with enhanced visible light photocatalytic activity. *RSC Adv.* **2017**, *7*, 37220–37229. [[CrossRef](#)]

28. Ong, C.B.; Ng, L.Y.; Mohammad, A.W. A review of ZnO nanoparticles as solar photocatalysts: Synthesis, mechanisms and applications. *Renew. Sustain. Energy Rev.* **2018**, *81*, 536–551. [[CrossRef](#)]
29. Raizada, P.; Sudhaik, A.; Patial, S.; Hasija, V.; Khan, A.A.P.; Singh, P.; Gautam, S.; Kaur, M.; Nguyen, V.-H. Engineering nanostructures of CuO-based photocatalysts for water treatment: Current progress and future challenges. *Arab. J. Chem.* **2020**, *13*, 8424–8457. [[CrossRef](#)]
30. Sobhani, A.; Alinavaz, S. ZnMn₂O₄ nanostructures: Synthesis via two different chemical methods, characterization, and photocatalytic applications for the degradation of new dyes. *Heliyon* **2023**, *9*, e21979. [[CrossRef](#)]
31. Abel, M.J.; Pramohtkumar, A.; Senthilkumar, N.; Jothivenkatachalam, K.; Inbaraj, P.F.H.; Joseph prince, J. Flake-like CuMn₂O₄ nanoparticles synthesized via co-precipitation method for photocatalytic activity. *Phys. B Condens. Matter* **2019**, *572*, 117–124.
32. Wirunchit, S.; Charoonsuk, T.; Vittayakorn, N. Facile sonochemical synthesis of near spherical barium zirconate titanate (BaZr_{1-y}Ti_yO₃; BZT); perovskite stability and formation mechanism. *RSC Adv.* **2015**, *5*, 38061–38074. [[CrossRef](#)]
33. Alias, F.I.H.; Rajmi, R.; Maulud, M.F.; Mohamed, Z. Structural, optical and dielectric properties of tellurium-based double perovskite Sr₂Ni_{1-x}Zn_xTeO₆. *RSC Adv.* **2021**, *11*, 31631–31640. [[CrossRef](#)]
34. Salem, B.B.; Essalah, G.; Ameer, S.B.; Duponchel, B.; Guermazi, H.; Guermazi, S.; Leroy, G. Synthesis and comparative study of the structural and optical properties of binary ZnO-based composites for environmental applications. *RSC Adv.* **2023**, *13*, 6287–6303. [[CrossRef](#)]
35. Mahroug, A.; Boudjadar, S.; Hamrit, S.; Guerbous, L. Structural, optical and photocurrent properties of undoped and Al-doped ZnO thin films deposited by sol-gel spin coating technique. *Mater. Lett.* **2014**, *134*, 248–251. [[CrossRef](#)]
36. Anand, A.M.; Raj, A.; Salam, J.A.; Nath, R.A.; Jayakrishnan, R. Photoconductivity in self-assembled CuO thin films. *Mater. Renew. Sustain. Energy* **2024**, *13*, 45–58. [[CrossRef](#)]
37. Wang, X.; Xu, C.; Liu, J. Extracting optical parameters of Cu-Mn-Fe spinel oxide nanoparticles for optimizing air-stable, high-efficiency solar selective coatings. *ACS Appl. Opt. Mater.* **2023**, *1*, 960–972. [[CrossRef](#)]
38. Sukriti; Chand, P.; Singh, V. Enhanced visible-light photocatalytic activity of samarium-doped zinc oxide nanostructures. *J. Rare Earths* **2020**, *38*, 29–38. [[CrossRef](#)]
39. Wang, J.; Liu, C.; Tong, L.; Li, J.; Luo, R.; Qi, J.; Li, Y.; Wang, L. Iron-copper bimetallic nanoparticles supported on hollow mesoporous silica spheres: An effective heterogeneous Fenton catalyst for orange II degradation. *RSC Adv.* **2015**, *5*, 69593–69605. [[CrossRef](#)]
40. Peng, F.; Lai, Q.; Chang, W.; Cui, Y. Preparation, characterization and visible light photocatalytic activities of samarium-doped mixed crystalline phase TiO₂ nanoparticles. *IOP Conf. Ser. Mater. Sci. Eng.* **2019**, *562*, 012031. [[CrossRef](#)]
41. Dash, D.; Panda, N.R.; Sahu, D. Sm³⁺ driven enhancement in photocatalytic degradation of hazardous dyes and photoluminescence properties of hexagonal-ZnO nanocolumns. *Nano Ex.* **2021**, *2*, 010007. [[CrossRef](#)]
42. Alzahrani, F.M.A.; Anwar, M.; Farooq, A.; Alrowaili, Z.A.; Al-Buriah, M.S.; Warsi, M.F. A new BiOCl-ZnFe₂O₄/CNTs ternary composite for remarkable photocatalytic degradation studies of a herbicide and a diazo dye. *Opt. Mater.* **2024**, *148*, 114876. [[CrossRef](#)]
43. Yu, F.; Cui, J.; Zhou, Y.; Li, Y.; Liu, Z.; He, L.; Zhang, J.; Tang, X.; Liu, Y. Structural and optical properties of ultra-thin g-C₃N₄ nanotubes based g-C₃N₄/Ag/Ag₂CrO₄ ternary composite photocatalyst with Z-scheme carrier transfer mechanism. *Opt. Mater.* **2021**, *121*, 111608. [[CrossRef](#)]
44. Asif, N.; Shehzadi, S.; Fatima, S.; Fatma, T. Photocatalytic Degradation of Synthetic Dyes Using Cyanobacteria-Derived Zinc Oxide Nanoparticles. *BioNanoSci.* **2023**, *13*, 365–375. [[CrossRef](#)]
45. Isai, K.A.; Shrivastava, V.S. Photocatalytic degradation of methylene blue using ZnO and 2%Fe-ZnO semiconductor nanomaterials synthesized by sol-gel method: A comparative study. *SN Appl. Sci.* **2019**, *1*, 1247. [[CrossRef](#)]
46. Aroob, S.; Carabineiro, S.A.C.; Taj, M.B.; Bibi, I.; Raheel, A.; Javed, T.; Yahya, R.; Alelwani, W.; Verpoort, F.; Kamwilaisak, K.; et al. Green Synthesis and Photocatalytic Dye Degradation Activity of CuO Nanoparticles. *Catalysts* **2023**, *13*, 502. [[CrossRef](#)]
47. Truong, T.T.; Pham, T.T.; Truong, T.T.T.; Pham, T.D. Synthesis, characterization of novel ZnO/CuO nanoparticles, and the applications in photocatalytic performance for rhodamine B dye degradation. *Environ. Sci. Pollut Res.* **2022**, *29*, 22576–22588. [[CrossRef](#)]
48. George, A.; Raj, D.M.A.; Venci, X.; Raj, A.D.; Irudayaraj, A.A.; Josephine, R.L.; Sundaram, S.J.; Al-Mohaimed, A.M.; Al Farraj, D.A.; Chen, T.-W.; et al. Photocatalytic effect of CuO nanoparticles flower-like 3D nanostructures under visible light irradiation with the degradation of methylene blue (MB) dye for environmental application. *Environ. Res.* **2022**, *203*, 111880. [[CrossRef](#)]
49. Sobhani, A. Hydrothermal synthesis of CuMn₂O₄/CuO nanocomposite without capping agent and study its photocatalytic activity for elimination of dye pollution. *Int. J. Hydrog. Energy* **2022**, *47*, 20138–20152. [[CrossRef](#)]
50. Saravanan, R.; Karthikeyan, S.; Gupta, V.K.; Sekaran, G.; Narayanan, V.; Stephen, A. Enhanced photocatalytic activity of ZnO/CuO nanocomposite for the degradation of textile dye on visible light illumination. *Mater. Sci. Eng. C* **2013**, *33*, 91–98. [[CrossRef](#)]
51. Alsulmi, A.; Mohammed, N.N.; Soltan, A.; Messih, M.F.A.; Ahmed, M.A. Engineering S-scheme CuO/ZnO heterojunctions sonochemically for eradicating RhB dye from wastewater under solar radiation. *RSC Adv.* **2023**, *13*, 13269–13281. [[CrossRef](#)]
52. Saadi, H.; Rhouma, F.I.H.; Benzarti, Z.; Bougrioua, Z.; Guermazi, S.; Khirouni, K. Electrical conductivity improvement of Fe doped ZnO nanopowders. *Mater. Res. Bull.* **2020**, *129*, 110884. [[CrossRef](#)]

53. Khan, R.; Zulfiqar; de Araujo, C.I.L.; Khan, T.; Muneeb-Ur-Rahman; Zia-Ur-Rehman; Khan, A.; Ullah, B.; Fashu, S. Influence of oxygen vacancies on the structural, dielectric, and magnetic properties of (Mn, Co) co-doped ZnO nanostructures. *J. Mater. Sci. Mater. Electron.* **2018**, *29*, 9785–9795. [[CrossRef](#)]
54. Bendahhou, A.; Chourti, K.; Loutou, M.; El Barkany, S.; Abou-Salama, M. Impact of rare earth ($RE^{3+} = La^{3+}, Sm^{3+}$) substitution in the A site perovskite on the structural, and electrical properties of $Ba(Zr_{0.9}Ti_{0.1})O_3$ ceramics. *RSC Adv.* **2022**, *12*, 10895–10910. [[CrossRef](#)]
55. Ishaque, M.Z.; Zaman, Y.; Arif, A.; Siddique, A.B.; Shahzad, M.; Ali, D.; Aslam, M.; Zaman, H.; Faizan, M. Fabrication of ternary metal oxide (ZnO:NiO:CuO) nanocomposite heterojunctions for enhanced photocatalytic and antibacterial applications. *RSC Adv.* **2023**, *13*, 30838–30854. [[CrossRef](#)]

Disclaimer/Publisher’s Note: The statements, opinions and data contained in all publications are solely those of the individual author(s) and contributor(s) and not of MDPI and/or the editor(s). MDPI and/or the editor(s) disclaim responsibility for any injury to people or property resulting from any ideas, methods, instructions or products referred to in the content.